Nanoscale Horizons

ROYAL SOCIETY OF CHEMISTRY

COMMUNICATION

View Article Online
View Journal | View Issue



Cite this: *Nanoscale Horiz.*, 2023, 8, 338

Received 19th September 2022,
Accepted 23rd December 2022

DOI: 10.1039/d2nh00431c

rsc.li/nanoscale-horizons



# Surface oxidation protection strategy of $CoS_2$ by $V_2O_5$ for electrocatalytic hydrogen evolution reaction†‡

Jie Wu,§[ab] Xuetao Qin,§[c] Yu Xia,§[de] Yuanyuan Zhang,[b] Bin Zhang,[b] Yunchen Du,[b] Hsing-Lin Wang,*[d] Siwei Li*[bf] and Ping Xu*[b]

**Transition metal sulfides (TMSs) are promising electrocatalysts for hydrogen evolution reaction (HER), while TMSs usually suffer from inevitable surface oxidation in air, and the impact of the surface oxidation on their HER catalytic activity remains unclear. Herein, we demonstrate an effective strategy for reducing the surface oxidation degree of easily oxidized $CoS_2$ by introducing glued vanadium pentoxide ($V_2O_5$) nanoclusters, taking advantage of the preferential adsorption and strong interaction between high-valence V and $O_2$. Combining oxidation protection and elaborate oxidation control experiments reveal that reduced surface oxidation degree of $CoS_2$ is conducive to affording promising HER catalytic performance, as the oxidized surface of $CoS_2$ can hinder the dissociation of water and thus is harmful to the HER process. Direct evidence is provided that surface oxidation should be carefully considered for TMS-based HER catalysts. The present work not only develops a new strategy for protecting $CoS_2$ from surface oxidation, but also provides deep insight into the impact of surface oxidation on the HER performance of transition metal compounds.**

### New concepts

Transition metal sulfides (TMSs) are important catalytic materials being widely used in the field of electrocatalysis, photocatalysis and thermal catalysis. Surface of TMSs can be easily oxidized under ambient conditions, however, the impact of the inevitable surface oxidation on the catalytic performance of TMSs has been always ignored. What's worse, efficient strategy for preventing TMSs from serious surface oxidation, crucial for academic and even industrial field, has not been developed. Herein, a novel strategy for preventing multiple TMSs from serious surface oxidation has been developed by introducing amorphous $V_2O_5$ clusters with close affinity to oxygen. Taking electrochemical hydrogen evolution reaction (HER) as a model reaction, the huge impact of the surface oxidation degree on the catalytic performance of TMSs has been shown clearly. We believe this work can not only arouse the attention on the surface oxidation of TMSs-based catalyst, but also provide a useful strategy for the surface protection of transition metal compounds including but not limited to TMSs.

## Introduction

Hydrogen evolution reaction (HER) is the cathodic reaction of water electrolysis, which is recognized as an important and sustainable approach to hydrogen production as clean fuels and chemical feedstocks.[1,2] Pt-based materials exhibit excellent activity for HER, but their high cost and scarcity limit the wide-spread applications.[3,4] Transition metal sulfides (TMSs) have been widely explored as a class of non-noble metal-based HER catalysts due to their unique physical and chemical properties.[5,6] Both layered $MS_2$ (*e.g.* $MoS_2$[7] and $WS_2$[8] and non-layered $M_xS_y$ (*e.g.* $CoS_2$,[9] $FeS_2$[10] and $Ni_3S_2$,[11] *etc.*) exhibit outstanding catalytic performance towards the HER, which are comparable or even superior to commercial Pt/C. Notably, multiple factors can impact the HER activity of TMSs, such as metal elements, ratios of metals and S atoms, vacancies, and electronic structures.[12,13] However, the impact of inevitable surface oxidation of TMSs on their HER performance has been paid less attention.

Like many TM compounds (*e.g.* carbides,[14,15] nitrides[16,17] and phosphides[18,19]), surface of TMSs can be easily oxidized under ambient conditions. In fact, the phenomenon that TMSs

[a] *National Engineering Laboratory for VOCs Pollution Control Technology and Equipment, School of Environment and Energy, South China University of Technology, Guangzhou 510640, China. E-mail: yhwj1105914174@foxmail.com*
[b] *MIIT Key Laboratory of Critical Materials Technology for New Energy Conversion and Storage, School of Chemistry and Chemical Engineering, Harbin Institute of Technology, Harbin 150001, China. E-mail: pxu@hit.edu.cn*
[c] *Beijing National Laboratory for Molecular Sciences, College of Chemistry and Molecular Engineering and College of Engineering, and BIC-ESAT, Peking University, Beijing 100871, China. E-mail: xuetaoqin@pku.edu.cn*
[d] *Department of Materials Science and Engineering, Southern University of Science and Technology, Shenzhen 518055, China. E-mail: wangxl3@sustech.edu.cn*
[e] *School of Physics and Astronomy, University of Birmingham, Edgbaston, Birmingham B152TT, UK. E-mail: 11856005@mail.sustech.edu.cn*
[f] *Institute of Industrial Catalysis, School of Chemical Engineering and Technology, Xi'an Jiaotong University, Xi'an 710049, China. E-mail: lisiwei@xjtu.edu.cn*

† Dedicated to the 120th anniversary of Southeast University.

‡ Electronic supplementary information (ESI) available: Fig. S1–S23. See DOI: https://doi.org/10.1039/d2nh00431c

§ These authors contributed equally to this work.

are susceptible to surface oxidation has been widely discovered and reported for almost all kinds of TMSs, though the degree of surface oxidation depends on the kinds of metal and crystalline phase.[20–23] For example, surface oxidation degree of $CoS_2$ calculated based on X-ray photoelectron spectroscopy (XPS) increases from ~20% to ~90% only after 8 days exposure to air at room temperature.[24] In contrast, the surface oxidation degree of $CoS_2$, with the same metallic element as $CoS_2$, only increases from 10% to 20% under the same condition. Furthermore, the surface oxidation of $MoS_2$ is even too slight to be tested by some well-known surface sensitive characterization techniques such as XPS, which can only be detected by scanning tunneling microscopy.[20,24] To the best of our knowledge, most of the current works on this topic have not carefully considered the surface oxidation, and theoretical calculations based on the intrinsic TMS model are performed to explain the structure–performance relationship and catalytic mechanism. In our view, this is not rigorous for the easily oxidized TMSs (*e.g.* $CoS_2$).

Since the importance of surface oxidation of TMSs has not been paid enough attention, efficient strategy for preventing TMSs from serious surface oxidation, crucial for academic and even industrial field, has not been developed. High-valence early transition metals (*e.g.* V) have close affinity to O due to the characteristic of strong metal–O bonds,[25,26] and therefore can be used to stabilize the structure of the catalyst under the oxidative condition. Inspired by this strategy, herein we develop a new method for reducing the surface oxidation degree of easily oxidized $CoS_2$ by introducing glued $V_2O_5$ nanoclusters (marked as $CoS_2$–$V_2O_5$). The structure and surface oxidation degree of $CoS_2$ have been investigated by using electron microscopic and spectroscopic characterizations. Moreover, the impact of the surface oxidation degree of $CoS_2$ on the HER performance are explored through control oxidation experiments. This work provides a new method to protect the surface oxidation of TMS, and investigates the influence of the surface oxidation on the electrocatalytic HER performance of $CoS_2$.

## Results

The synthesis process of $CoS_2$–$V_2O_5$ supported on carbon cloth (CC) is shown in Fig. 1. Firstly, CC supported Co zeolitic imidazolate frameworks (marked as Co MOFs) were immersed in $Na_3VO_4$ solution to get $Co_3V_2O_8$–Co MOFs intermediate *via* ion exchange process (Fig. S1–S7, ESI‡). Subsequently, the $Co_3V_2O_8$–Co MOFs was subjected to mild sulfidation at 400 °C under Ar atmosphere to obtain the $CoS_2$–$V_2O_5$ catalyst. The $Co_3V_2O_8$–Co MOFs intermediate with highly mixed Co and V elements may be a key factor for the generation of highly dispersed $V_2O_5$ nanoclusters around $CoS_2$. For comparison, the $CoS_2$ catalyst was synthesized *via* the same sulfidation treatment by directly using Co MOFs as the precursor (Fig. S8 and S9, ESI‡).

X-ray diffraction (XRD) was carried to study the structures of the as-synthesized samples (Fig. 2a). The XRD pattern of as-synthesized $CoS_2$ matches well with the standard cubic $CoS_2$

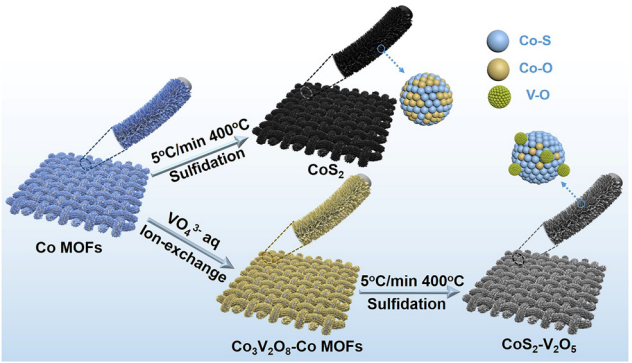


Fig. 1 Schematic illustration of the synthesis strategy of $CoS_2$ and $CoS_2$–$V_2O_5$ nanoarrays supported on carbon cloth (CC).

crystal phase (JCPDS No. 41-1471). However, for the V-incorporated $CoS_2$ sample, only diffraction peaks assigned to $CoS_2$ appear because V species cannot be detected by XRD due to low crystallinity and small particle size. The chemical composition of the V species was further investigated by using X-ray absorption fine structure (XAFS). The V K-edge X-ray absorption near-edge spectroscopy (XANES)of the as-synthesized sample is drastically similar to that of $V_2O_5$ (Fig. 2b), suggesting the formation of $CoS_2$–$V_2O_5$. Moreover, the bonding structures of V species were carried out by extend X-ray absorption fine structure (EXAFS, Fig. 2c). There are only V–O (1.56 Å) and

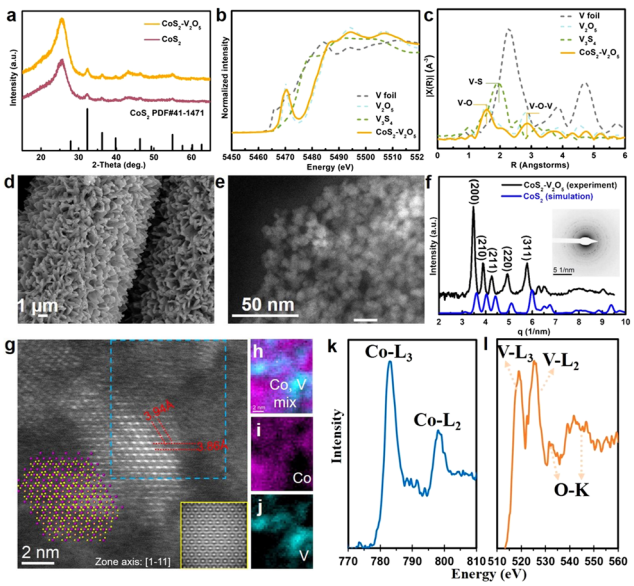


Fig. 2 Structural analysis of $CoS_2$–$V_2O_5$. (a) XRD patterns of $CoS_2$ and $CoS_2$–$V_2O_5$, (b) V K-edge XANES of $CoS_2$–$V_2O_5$, V foil, $V_2O_5$ and $V_3S_4$, (c) V K-edge EXAFS of $CoS_2$–$V_2O_5$, V foil, $V_2O_5$ and $V_3S_4$, (d) SEM image of $CoS_2$–$V_2O_5$ nanoarrays loaded on CC, (e) HAADF-STEM image of $CoS_2$–$V_2O_5$ particles, (f) radial intensity profile of $CoS_2$–$V_2O_5$ (black line) and the simulated radial intensity profile of $CoS_2$ (blue line), inset shows the SAED of $CoS_2$–$V_2O_5$, (g) atomic HAADF-STEM image of $CoS_2$–$V_2O_5$ along with the zone axis [1–11] direction (inset shows the atomic model of $CoS_2$), (h) cobalt and vanadium colormix, (i) cobalt mapping, (j) vanadium mapping, EELS spectra of k cobalt L edge, (l) oxygen K edge, and vanadium L edge acquired from the blue rectangular region in (g).

V–O–V (2.83 Å) scatterings in the V K-edge EXAFS spectra of $CoS_2$–$V_2O_5$, while the V–S scattering (1.97 Å) is absent. This is a direct evidence for the existence of vanadium oxides in the as-synthesized $CoS_2$–$V_2O_5$ heterostructure.

The morphology and crystallinity of the $CoS_2$–$V_2O_5$ heterostructure were further investigated by electron microscopy. The scanning electron microscopy (SEM) shows the similar nanoarray morphology to that of the Co MOFs precursor and $Co_3V_2O_8$–Co MOFs intermediate (Fig. 2d and Fig. S1, ESI‡). Upon closer observation by the high-angle annular dark-field scanning transmission electron microscopy (HAADF-STEM) image in Fig. 2e, the nanoarray grown on the carbon cloth consists of $CoS_2$–$V_2O_5$ nanoparticles that are about 8 nm in size. Notably, the integrated radial intensity profile (Fig. 2f) extracted from the selected area electron diffraction (SAED) corresponding to Fig. 2e is similar to the simulated radial intensity profile of $CoS_2$, where no peak can be attributed to $V_2O_5$, which indicates that the $V_2O_5$ is amorphous in nature.

Aberration corrected STEM and corresponding electron energy loss spectrum (EELS) were further employed to characterize the structure of $CoS_2$–$V_2O_5$. The atomic resolution image of $CoS_2$ is presented in Fig. 2g with the zone axis [1−11]. The measured lattice spacings of 3.94 Å and 3.86 Å indicate (110) and (0−11) planes with an angle of 120°. The simulated HAADF-STEM image of $CoS_2$ (110) facets with a *d*-spacing of 3.92 Å is presented at the bottom right corner of Fig. 2g, matching well with the atomic model of $CoS_2$ with (110) planes (inset in Fig. 2g).[27] More importantly, an area marked by the blue dashed rectangle in the STEM image was scanned for collecting the EEL spectra of V and Co elements to map the distribution of Co and V. As shown in Fig. 2h–j, Co and V elements were separated in space. Moreover, the low magnification mappings (Fig. S10, ESI‡) can also indicate that $V_2O_5$ was adhered on the surface of $CoS_2$ nanoparticles, with the size about 1–2 nm. As the amorphous $V_2O_5$ has been confirmed according to the previous characterizations, $V_2O_5$ nanoclusters (1–2 nm) are glued to the crystalline $CoS_2$ nanoparticles. The valence of V and Co were also analyzed from the EEL spectra (Fig. 2k–l). The peak intensity of V-$L_3$ (518.8 eV) is lower than that of V-$L_2$ (526.1 eV) with a ratio of $L_3/L_2$ = 0.7, indicating the valence of vanadium oxides in the as-synthesized sample is +5,[28] consistent to the XANES result. The calculated Co-$L_3/L_2$ ratio of 3 reveals that the valence of Co in the $CoS_2$ is a mixture of +2 and +3.[29]

Based on the above characterizations, the as-prepared $CoS_2$–$V_2O_5$ heterostructure is composed of crystalline $CoS_2$ nanoparticles around with amorphous $V_2O_5$ nanoclusters. The homogeneously distribution of $V_2O_5$ and $CoS_2$ at nanoscale is a key to the surface oxidation protection due to the formation of abundant $CoS_2$–$V_2O_5$ interfaces.

To demonstrate the surface oxidation protection effect of $V_2O_5$ nanoclusters, the surface oxidation degree of the $CoS_2$ and $CoS_2$–$V_2O_5$ samples is investigated by using spectroscopic characterizations and control experiments (Fig. 3). Raman spectrum of $CoS_2$ sample (Fig. 3a) shows peaks centered at ∼487, 529, 600 and 698 $cm^{-1}$ corresponding to the $E_g$, $F_{2g}$, $F_{2g}$ and $A_{1g}$

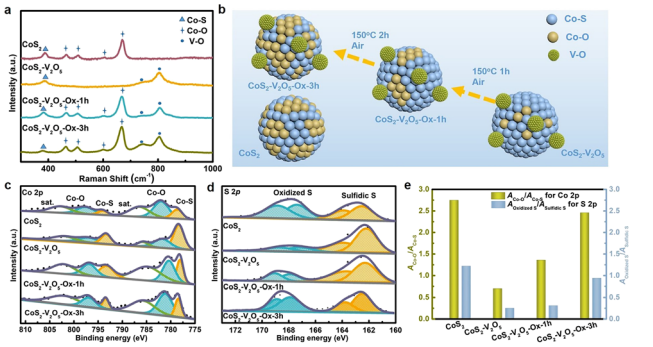


Fig. 3 (a) Raman spectra of $CoS_2$, $CoS_2$–$V_2O_5$, $CoS_2$–$V_2O_5$-Ox-1h and $CoS_2$–$V_2O_5$-Ox-3h, in which Ox means a control oxidation process in Air at 150 °C, (b) schematic illustration of surface oxidation phenomenon of $CoS_2$, comparison of (c) Co 2p and (d) S 2p XPS spectra of $CoS_2$, $CoS_2$–$V_2O_5$, $CoS_2$–$V_2O_5$-Ox-1h and $CoS_2$–$V_2O_5$-Ox-3h, and (e) the ratios of $A_{Co-O}:A_{Co-S}$ and $A_{Oxidized\ S}:A_{Sulfidic\ S}$, in which *A* represents the peak area in the XPS spectra.

modes of Co–O species, respectively,[30] whereas the peak centered at 382 $cm^{-1}$ is identified as the $A_g$ mode of Co–S species.[31] The appearance of the Co–O species in the Raman spectrum have been reported to result from the surface oxidation of $CoS_2$ in air.[32] As seen from the Raman spectrum, the as-reported HER performance for $CoS_2$ has been heavily affected by the spontaneous surface oxidation, which may not reflect its catalytic activity. In contrast, the peaks assigned to Co–O species disappear in the Raman spectrum of the $CoS_2$–$V_2O_5$ sample. Instead, two peaks for V–O species (centered at 743 and 806 $cm^{-1}$) emerge along with the peaks for Co–S species.[33,34] This result implies that the surface oxidation degree of $CoS_2$ is significantly reduced upon the introduction of $V_2O_5$ nanoclusters.

Even though the $CoS_2$–$V_2O_5$ and $CoS_2$ catalysts have different surface oxidation degree, it is not enough to compare their HER performance to show the impact of surface oxidation. Therefore, we carried out a control oxidation experiments for the $CoS_2$–$V_2O_5$ (Fig. 3b) to obtain more control groups with different surface oxidation degree. Specifically, the $CoS_2$–$V_2O_5$ was oxidized in air at 150 °C for different time periods to tune the surface oxidation degree of $CoS_2$, which were marked as $CoS_2$–$V_2O_5$-Ox-1h and $CoS_2$–$V_2O_5$-Ox-3h, respectively. XRD patterns and SEM images of the control groups (Fig. S8 and S9, ESI‡) tell that the crystalline structures and morphologies of these oxidized samples almost keep unchanged. However, as seen in Fig. 3a, the four peaks assigned to Co–O peaks appear clearly in the Raman spectra of $CoS_2$–$V_2O_5$-Ox-1h and $CoS_2$–$V_2O_5$-Ox-3h, indicating that controlled surface oxidation of $CoS_2$ has been successfully realized.

XPS was further employed to investigate the surface oxidation degree of the above four samples. There are only Co, V (absent for the $CoS_2$ sample), O, S, C, and N elements in the survey spectra, indicating the purity of the as-synthesized samples (Fig. S11, ESI‡). In the V 2p spectra of the $CoS_2$–$V_2O_5$ and the oxidized samples, the peaks centered at 517.5 and 524.8 eV are assigned to V(+ 5) species (Fig. S12, ESI‡).[35] The Co 2p spectra of the samples can be divided into three couples of peaks (Fig. 3c). Specifically, the peaks centered at 778.7 and 794 eV are assigned

 

to the Co–S species, whereas the peaks at 782, 797.6, 786.5 and 803 eV are assigned to the Co–O species and the corresponding satellite peaks.[36] For the $CoS_2$ sample, the peak intensity of Co–O is relatively higher than that of Co–S, indicating the serious surface oxidation of $CoS_2$. The area ratio of Co–O and Co–S ($A_{Co-O}:A_{Co-S}$), which can reflect the surface oxidation degree of $CoS_2$, is calculated to be 2.75 for $CoS_2$. For $CoS_2$–$V_2O_5$, both Co–S and Co–O species can be detected in the Co 2p spectrum, because XPS is more sensitive to the surface species than Raman spectroscopy. The intensity of Co–O is much lower than that of Co–S and the value of $A_{Co-O}:A_{Co-S}$ decreases sharply to 0.7, a strong proof that the surface oxidation of $CoS_2$ is effectively reduced with the introduction of $V_2O_5$ nanoclusters. Furthermore, the peaks of Co–S for $CoS_2$–$V_2O_5$ are located at 778.18 and 793.08 eV, which are negatively shifted compared with $CoS_2$, suggesting the construction of $CoS_2$–$V_2O_5$ heterojunction structure. When the $CoS_2$–$V_2O_5$ is oxidized in air, the peak intensity of Co–O increases, while the peak intensity of Co–S decreases. The $A_{Co-O}:A_{Co-S}$ are calculated to be 1.36 and 2.46 for the $CoS_2$–$V_2O_5$-Ox-1h and $CoS_2$–$V_2O_5$-Ox-3h, respectively.

The above analyses based on the Co 2p spectra can be further supported by the S 2p spectra of these samples (Fig. 3d). In brief, both oxidized S and sulfidic S species can be found in all the S 2p spectra of $CoS_2$, $CoS_2$–$V_2O_5$, $CoS_2$–$V_2O_5$-Ox-1h and $CoS_2$–$V_2O_5$-Ox-3h, and the ratio of $A_{Oxidized\ S}:A_{Sulfidic\ S}$ is calculated to be 1.22, 0.25, 0.31 and 0.94, respectively, following the same trend as $A_{Co-O}:A_{Co-S}$ (Fig. 3e).

Three major conclusions about the surface oxidation of $CoS_2$ can be drawn according to the above Raman and XPS results. 1) As reported, $CoS_2$ suffers from serious surface oxidation in air. 2) Construction of the $CoS_2$–$V_2O_5$ hybrid materials can significantly reduce the surface oxidation degree of $CoS_2$. 3) The control oxidation experiment of $CoS_2$–$V_2O_5$ can tune the surface oxidation degree, which is helpful to understand the effect of surface oxidation on the HER performance of $CoS_2$.

The electrocatalytic performance of CC, commercial Pt/C, $CoS_2$, $CoS_2$–$V_2O_5$ as well as the control samples towards the HER was tested in alkaline media (1 M KOH). The reference electrode is calibrated experimentally (Fig. S13, ESI‡).[37] As shown in the iR-corrected linear sweep voltammetry (LSV, Fig. 4a) curves, bare CC shows very poor catalytic performance towards HER. The $CoS_2$ exhibits much better catalytic performance towards HER, requiring an overpotential of 272 mV to deliver a current density of 10 mA $cm^{-2}$. Significantly, once the $CoS_2$–$V_2O_5$ heterostructure is fabricated, the required overpotential is sharply reduced to 128 mV at 10 mA $cm^{-2}$. Moreover, $CoS_2$–$V_2O_5$ affords a mass activity of 0.71 A $g^{-1}$ at an overpotential of 100 mV (Fig. S14, ESI‡), which is much higher than that of $CoS_2$ (0.18 A $g^{-1}$). Interestingly, when the $CoS_2$–$V_2O_5$ samples are oxidized for 1 h and 3 h, the HER performances drop gradually, requiring an overpotential of 166 and 196 mV at 10 mA $cm^{-2}$, respectively.

To further understand the impact of surface oxidation on the HER performance of $CoS_2$-based catalysts, we plot the overpotential of the above $CoS_2$–$V_2O_5$ and $CoS_2$ catalysts as a function of the $A_{Co-O}:A_{Co-S}$ from XPS (Fig. 4b). For the

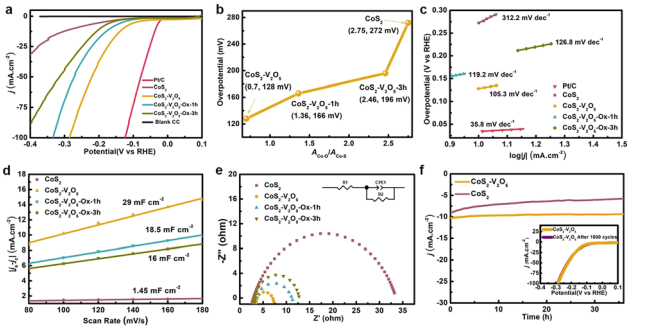


Fig. 4 HER performance of the as-prepared electrocatalysts in 1 M KOH solution. (a) LSV curves after *iR* correction in comparison to Pt/C, (b) the relationship between $A_{Co-O}/A_{Co-S}$ and the overpotential at 10 mA $cm^{-2}$, (c) Tafel plots, (d) $C_{dl}$ extracting from the CV curves, (e) EIS spectra (inset shows the equivalent circuit used to simulate the Nyquist plots), and (f) long-time stability of $CoS_2$–$V_2O_5$ for 36 h (inset exhibits the LSV curves before and after 1000 CV cycles test).

$CoS_2$–$V_2O_5$ and $CoS_2$–$V_2O_5$-Ox samples, the overpotential increases almost linearly with surface oxidation degree from 128 to 196 mV, suggesting the surface oxidation degree is the dominant role for the different HER performance of these samples. The overpotential increases sharply for the $CoS_2$ catalyst (272 mV), implying that the $V_2O_5$ nanoclusters in the heterostructure may also contributes to the catalytic process. In sum, the lower surface oxidation degree of $CoS_2$, the better HER performance.

Furthermore, the HER kinetics of the $CoS_2$-based catalysts are informed from the corresponding Tafel plots in Fig. 4c. The Tafel slope of $CoS_2$–$V_2O_5$ is 105.3 mV $dec^{-1}$, which is smaller than that of $CoS_2$ (312.2 mV $dec^{-1}$), $CoS_2$–$V_2O_5$-Ox-1h (119.2 mV $dec^{-1}$) and $CoS_2$–$V_2O_5$-Ox-3h (126.8 mV $dec^{-1}$), indicating the facilitated reaction kinetics during HER process over $CoS_2$–$V_2O_5$. Additionally, electrochemical double layer capacitance ($C_{dl}$) is obtained from the cyclic voltammetry (CV) curves at different scan rates in the non-faradaic potential range (Fig. 4d and Fig. S15, ESI‡), which is an important parameter to derive the electrochemically active surface area (ECSA).[38] As the construction of $CoS_2$–$V_2O_5$ heterojunction structure, which is considered to effectively improve the capacitance performance[39,40] and as the more catalytical active sites (Co–S) are maintained due to the protection of $V_2O_5$, the $CoS_2$–$V_2O_5$ owns the highest ECSA (725 $cm^2$, Fig. S16, ESI‡). Thus, the $CoS_2$–$V_2O_5$ owns the highest $C_{dl}$ (29 mF $cm^{-2}$) according to the equation ECSA = $C_{dl}/C_s$, in which $C_{dl}$ is positively correlated to ECSA. As shown in Fig. S17 (ESI‡), we also conducted the turn over frequency (TOF) of $CoS_2$ and $CoS_2$–$V_2O_5$. The TOF values of $CoS_2$ and $CoS_2$–$V_2O_5$ are 0.13 $s^{-1}$ and 0.08 $s^{-1}$ at the overpotential of 150 mV, indicating the better intrinsic catalytic activity of $CoS_2$–$V_2O_5$, which is in accordance with $C_{dl}$ and ECSA results. Moreover, as has been reported, the interface between $CoS_2$ and $V_2O_5$ can accelerate the kinetics of HER process and promote electron transport and finally reduce the charge transfer resistance.[41] Thus, the electrochemical impedance spectroscopy (EIS) for these samples suggests that the charge transfer resistance for $CoS_2$–$V_2O_5$ (3.86 Ω) is much smaller than that of $CoS_2$ (31.24 Ω),

$CoS_2$–$V_2O_5$-Ox-1h (9.87 Ω) and $CoS_2$–$V_2O_5$-Ox-3h (8.46 Ω) (Fig. 4e), demonstrating the enhanced charge transfer efficiency and improved reaction kinetics of $CoS_2$–$V_2O_5$ during the HER process. And $CoS_2$–$V_2O_5$ catalyst is also demonstrated to have an excellent mass transport property (Fig. S18, ESI‡). Besides, the HER Faraday efficiency (FE) of $CoS_2$ and $CoS_2$–$V_2O_5$ were performed under the current of 10 mA $cm^{-2}$ for 6000 s, which were 98.1% and 98%, indicating the high selectivity during the HER process for both catalysts (Fig. S19, ESI‡).

The poor stability is a main drawback for $CoS_2$-based HER electrocatalyst. The chronoamperometric *i*–*t* curves at 10 mA $cm^{-2}$ of $CoS_2$ and $CoS_2$–$V_2O_5$ were conducted for 36 h (Fig. 4f). There is significant degradation of current density of $CoS_2$, whereas the *i*–*t* curve of $CoS_2$–$V_2O_5$ keeps stable. It means the lower surface oxidation degree may also help to improve the stability of $CoS_2$-based HER catalyst. Moreover, the LSV curve of $CoS_2$–$V_2O_5$ after 1000 CV cycles basically coincides with the initial one (Fig. 4f, inset). Both experiments indicate the excellent long-term stability of the $CoS_2$–$V_2O_5$ catalyst towards HER. The excellent stability of $CoS_2$–$V_2O_5$ can be attributed to the well-maintained morphology and maintained Co–S surface, which is confirmed by using SEM, TEM and XPS (Fig. S20 and S21, ESI‡). We have also carried out Co K-edge XANES and EXAFS of $CoS_2$ and $CoS_2$–$V_2O_5$ after HER tests to understand the different stability of these two catalysts. Both XANES and EXAFS (Fig. S22, ESI‡) show $CoS_2$ converts to cobalt (hydr)oxides, which is consistent to the reported literatures.[23] In contrast, the Co–S and Co–S–V bonds in EXAFS clearly show that $CoS_2$ in the $CoS_2$–$V_2O_5$ catalyst retain stable after HER test, which is also supported by XPS result (Fig. S21, ESI‡). The $V_2O_5$ clusters can not only reduce the surface oxidation degree of $CoS_2$ in air, but also keep it stable during HER by avoiding the bulk oxidation. It is the structural stability of $CoS_2$–$V_2O_5$ that leads to the outstanding stability and long-term durability of this catalyst.).

Density functional theory (DFT) calculations were carried out to understand why the $CoS_2$ with lower surface oxidation degree exhibits better catalytic performance for HER. As shown in Fig. 5a–c, $CoS_2$ (100) and O modified $CoS_2$ (100) (marked as $CoS_2$–O) were selected as the models for simplification according to XRD results. Moreover, $V_2O_5$ clusters on $CoS_2$ (100) are built to represent the $CoS_2$–$V_2O_5$ sample. Generally, the elemental HER steps in alkaline solution include $H_2O$ adsorption, $H_2O$ activation, H desorption and OH desorption.[42,43] The chemisorption models of reaction intermediates adsorbed on the (100) surface of $CoS_2$ (*$H_2O$, *OH–H and *OH) are displayed concretely in Fig. S23 (ESI‡). The standard free energy ($\Delta G$) diagrams for $CoS_2$ $CoS_2$–O and $CoS_2$–$V_2O_5$ of HER reaction steps are shown in Fig. 5d. For $CoS_2$, the Gibbs free energies of $H_2O$ adsorption and $H_2O$ dissociation are 0.37 and 0.67 eV, respectively, while the following steps are spontaneous. It can be learned that $H_2O$ dissociation is the rate determining step (RDS) for $CoS_2$. With the $CoS_2$ surface modified by O, although the $H_2O$ adsorption is effectively accelerated ($\Delta G$ = −0.05 eV), the energy barrier for $H_2O$ dissociation is even higher, resulting in a much higher $\Delta G_{RDS}$ of 1.56 eV. The above results clearly show that the surface

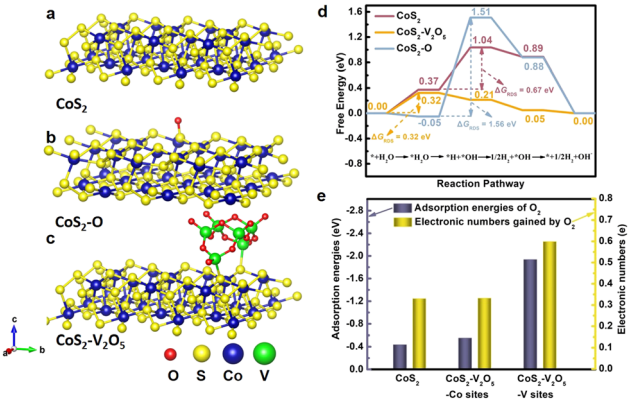


Fig. 5 (a–c) Crystal structures of $CoS_2$, $CoS_2$–O and $CoS_2$–$V_2O_5$, (d) comparison of standard Gibbs free energies at the rate determining step of $CoS_2$, $CoS_2$–O and $CoS_2$–$V_2O_5$ during the HER process, and (e) the adsorption energies of $O_2$ molecules at metal sites (Co sites and V sites) and the electronic numbers gained by $O_2$ molecules.

oxidation of $CoS_2$ is harmful to the HER process due to the hindering of $H_2O$ dissociation.

We further investigate the synergetic effect of $V_2O_5$ and $CoS_2$ through DFT calculations. The contribution of $V_2O_5$ to HER is highlighted by comparing $CoS_2$ and $CoS_2$–$V_2O_5$ models (the red and yellow line, Fig. R6, ESI‡). The introduction of $V_2O_5$ will not bring an obvious change for $H_2O$ adsorption, but it significantly accelerates the $H_2O$ dissociation, leading to a spontaneous process ($\Delta G$ = −0.11 eV). As a result, the $H_2O$ adsorption step becomes the RDS for $CoS_2$–$V_2O_5$, with a $\Delta G_{RDS}$ of 0.32 eV. The $\Delta G_{RDS}$ of $CoS_2$–$V_2O_5$ is lower than that of $CoS_2$, which means $CoS_2$–$V_2O_5$ possesses better catalytic activity for HER than $CoS_2$ from a theoretical point of view, matching well with the experimental results. Based on the theoretical calculations, the homogeneously distributed $V_2O_5$ can facilitate the dissociation of water and further the whole HER process. Therefore, the synergetic effect of $V_2O_5$ and $CoS_2$ include two parts. On one hand, $V_2O_5$ can reduce the surface oxidation of $CoS_2$ in air and the bulk oxidation of $CoS_2$ during HER, leading to exposed and stable Co–S sites for HER. On the other hand, $V_2O_5$ also contributes to the HER by facilitating the dissociation of water and further the whole HER process.

Another important issue is why the $V_2O_5$ nanoclusters can protect $CoS_2$ from surface oxidation. To answer this question, it is reasonable to investigate the adsorption and interaction between $O_2$ and the $CoS_2$ or $CoS_2$–$V_2O_5$ catalyst. $V_2O_5$ clusters on $CoS_2$ (100) were built to represent the $CoS_2$–$V_2O_5$ sample (Fig. 5c) and multiple theoretical methods were adopted. On one hand, the adsorption energy of $O_2$ molecule ($E_{O_2}$) on the $CoS_2$ (Co sites) and $CoS_2$–$V_2O_5$ (Co sites and V sites) was calculated (Fig. 5e, blue bar). $E_{O_2}$ of Co site in $CoS_2$ is calculated to be −0.436 eV, meaning the adsorption of $O_2$ is spontaneously. By contrast, $E_{O_2}$ of Co sites in the $CoS_2$–$V_2O_5$ is slightly reduced to −0.553 eV, which may result from the electronic interaction between the $CoS_2$ and $V_2O_5$ species. Significantly, $E_{O_2}$ of V sites in the $CoS_2$–$V_2O_5$ reaches −1.935 eV, much lower than that of Co sites. The results clearly indicate that $O_2$

 

molecule preferentially adsorbs on V sites rather than Co sites in the $CoS_2$–$V_2O_5$. On the other hand, Bader charge analysis was applied to explore the charge transfer process between metal sites and adsorbed $O_2$ molecules (Fig. 5e, yellow bar). The number of the transferred electron is 0.330 for Co sites in $CoS_2$ and 0.332 and 0.559 for Co sites and V sites in $CoS_2$–$V_2O_5$. The more transferred electron, the stronger interaction between $O_2$ and metal sites. According to the above calculations, $O_2$ molecules in air can preferentially adsorb on $V_2O_5$ rather than $CoS_2$ and interact strongly with the V sites rather than Co sites in the $CoS_2$–$V_2O_5$ catalyst. As a result, the $V_2O_5$ nanoclusters protect the $CoS_2$ nanoparticles from serious surface oxidation.

## Conclusions

In this work, we demonstrate a novel surface oxidation protection method for $CoS_2$ by introducing $V_2O_5$ nanoclusters, and systematically investigate the impact of surface oxidation on the HER performance. XAFS, HADDF-STEM and EELS demonstrate that amorphous $V_2O_5$ nanoclusters homogeneously glue to $CoS_2$ nanoparticles thanks to the MOFs-derived synthetic method, leading to significantly reduced surface oxidation degree of $CoS_2$ and excellent stability of $CoS_2$–$V_2O_5$ during HER by avoiding the bulk oxidation. The preferential adsorption and strong interaction between $O_2$ and $V_2O_5$ clusters help to protect $CoS_2$ from serious surface oxidation. As a result, $CoS_2$–$V_2O_5$ delivers a superior HER performance in alkaline media, requiring a low overpotential of 128 mV to deliver a current density of 10 mA $cm^{-2}$, which is much better than that of $CoS_2$ (272 mV). Through the control oxidation experiments of $CoS_2$–$V_2O_5$, it is demonstrated that the lower surface oxidation degree of $CoS_2$, the better HER performance. DFT calculations indicate that the surface oxidation of $CoS_2$ can hinder the dissociation of water, and the introduction of $V_2O_5$ can effectively facilitate the dissociation of water and further improve the HER process. This work shows the crucial impact of the surface oxidation of TMSs on their HER performance and provides a new idea for surface oxidation protection of $CoS_2$ that may be expanded to other TMSs and transition metal compounds.

## Experimental section

### Materials

Cobalt(II) nitrate hexahydrate ($CoNO_3{\cdot}6H_2O$), dimethyl imidazole ($C_4H_6N_2$), sodium orthovanadate ($Na_3VO_4$), sulfur powder (S), potassium hydroxide (KOH), iridium dioxide ($IrO_2$) and Nafion were all were purchased from Aladdin Industrial Corporation. Pt sheet was purchased from Aldrich. And deionized water (DI), absolute ethanol ($C_2H_5OH$). All chemicals were used directly without any purification treatment.

### Methods

**Synthesis of Co MOFs.** In the synthesis of Co MOFs, 0.582 g $CoNO_3{\cdot}6H_2O$ and 1.314 g $C_4H_6N_2$ were dissolved in 40 mL of DI water, which were stirred for 15 minutes rapidly in order to mix evenly. Then, the solution of $C_4H_6N_2$ was quickly poured into the cobalt ion solution, which was stirred for again 5 minutes. After that, stop stirring and put the hydrophilic CC into the above mixed solution. After standing for 4 hours under the ambient conditions, the CC covered with blue Co MOFs was taken out, and then was washed by water, alcohol. Finally, drying it under vacuum overnight.

**Synthesis of $Co_3V_2O_8$–Co MOFs.** During the typical production of $Co_3V_2O_8$–Co MOFs, ion-exchange method was employed to etch the fresh Co MOFs. The specific method is as follows. Firstly, we prepared the etching solution by dissolving 0.3 g $Na_3VO_4$ in 60 mL of deionized water through a warm water bath. Subsequently, Co MOFs were put into the above solution. By adjusting the etching time, the samples of incompletely etched ($Co_3V_2O_8$–Co MOFs) and fully etched ($Co_3V_2O_8$) are obtained. The Co etching time for $Co_3V_2O_8$–Co MOFs was 20 minutes.

**Synthesis of $CoS_2$–$V_2O_5$ and $CoS_2$.** $Co_3V_2O_8$–Co MOFs were submitted to sulfidation at 400 °C with the heating rate of 5 °C $min^{-1}$ under Ar inert atmosphere, producing $CoS_2$–$V_2O_5$. During the sulfidation process, 0.5 g S power was used as the sulfur source. Additionally, $CoS_2$ was also synthesized *via* the same sulfidation treatment only without the ion-exchange process.

**Characterization.** Rigaku D/MAXRC X-ray diffractometer (45.0 kV, 50.0 mA), equipped with the anticathode of Cu target, was used to collect XRD patterns. Quanta 200 S (FEI) and Tecnai F20 were used to take the scanning electron microscopic (SEM) and transmission electron microscopic (TEM) images, respectively. The X-ray energy dispersive spectroscopy (EDS) mappings were acquired by the microscope of FEI Talos™ F200X, working at 200 kV. The electron energy loss spectroscopy (EELS) was obtained under scanning transmission electron microscopy (STEM) mode at 300 kV using a Titan Themis G2 60-300 equipped with a monochromator and a probe corrector. The simulated STEM image of $CoS_2$ facets was generated using the kinematic scattering method, which is developed as a software running in Matlab. Before simulating, the atomic model of $CoS_2$ plane was built based on a cubic structure, whose space group is $Pa\bar{3}$. The software read the coordinates of Co and S atoms from the generated atomic model, creating the simulated image along with the direction of [1−11]. We used Renishaw in *Via* micro Raman spectroscopy system (laser wavelength: 532 nm) to record the Raman spectra. X-ray photoelectron spectra (XPS) were received by operating PHI 5700 ESCA system, in which an Al Kα radiation was used as a source ($h\nu$ = 1486.6 eV). The Fourier transform infrared spectroscopy (FT-IR) was received by operating with Tensor-27, Germany, Bruker system. The X-ray absorption fine structure spectra V K-edge were collected at 44A beamline of National Synchrotron Radiation Research Center (NSRRC) Taiwan.[44,45]

**Electrode preparation and electrochemical measurements.** Standard three-electrode system was carried to test the electrochemical performance of the as-prepared materials, in which the carbon rod, Hg/HgO and the electrode clip equipping with the catalysts were used as counter electrode, reference electrode

and working electrode, respectively. Furthermore, all the tests are carried out on CHI 660E workstation.

**Theoretical calculations.** At the DFT calculations part of this paper, the VASP software was conducted to perform the first-principles density functional theory calculation by the method of PAW.[46,47] In the calculation, the exchange functional is processed based on the PBE formula[48] and the generalized gradient approximation method.[49,50] The spin-polarized all results with a cut-off energy of 450 eV as the plane-wave basis set.

## Conflicts of interest

There are no conflicts to declare.

## Acknowledgements

This work was supported by the financial support from Natural Science Foundation of China (No. 21871065, and 22071038), China Postdoctoral Science Foundation Grant (No. 2020M670894), Heilongjiang Touyan Team (HITTY-20190033), and Interdisciplinary Research Foundation of HIT (IR2021205). Prof. Li acknowledges the financial support from the "Young Talent Support Plan" of Xi'an Jiaotong University (HG6J024), High-Level Innovation and Entrepreneurship Talent Project of Qinchuangyuan (QCYRCXM-2022-123) and "Young Talent Lift Plan" of Xi'an city (095920221352). We would like to express our great gratitude to the supercomputing center in Wuhan University.



## References

1 B. Zhu, R. Zou and Q. Xu, *Adv. Energy Mater.*, 2018, **8**, 1801193.
2 J. Zhu, L. Hu, P. Zhao, L. Lee and K. Wong, *Chem. Rev.*, 2020, **120**, 851–918.
3 D. Liu, X. Li, S. Chen, H. Yan, C. Wang, C. Wu, Y. Halleem, S. Duan, J. Lu, B. Ge, P. Ajayan, Y. Luo, J. Jiang and L. Song, *Nat. Energy*, 2019, **4**, 512–518.
4 E. Kemppainen, A. Bodin, B. Sebok, T. Pedersen, B. Seger, B. Mei, D. Bae, P. Vesborg, J. Halme, O. Hansen, P. Lund and I. Chorkendorff, *Energy Environ. Sci.*, 2015, **8**, 2991–2999.
5 Y. Guo, T. Park, J. Yi, J. Henzie, J. Kim, Z. Wang, B. Jiang, Y. Bando, Y. Sugahara, J. Tang and Y. Yamauchi, *Adv. Mater.*, 2019, **31**, e1807134.
6 H. Sun, Z. Yan, F. Liu, W. Xu, F. Cheng and J. Chen, *Adv. Mater.*, 2020, **32**, e1806326.
7 Y. Yin, J. Han, Y. Zhang, X. Zhang, P. Xu, Q. Yuan, L. Samad, X. Wang, Y. Wang, Z. Zhang, P. Zhang, X. Cao, B. Song and S. Jin, *J. Am. Chem. Soc.*, 2016, **138**, 7965–7972.
8 L. Cheng, W. Huang, Q. Gong, C. Liu, Z. Liu, Y. Li and H. Dai, *Angew. Chem., Int. Ed.*, 2014, **126**, 7994–7997.
9 S. Peng, L. Li, X. Han, W. Sun, M. Srinivasan, S. Mhaisalkar, F. Cheng, Q. Yan, J. Chen and S. Ramakrishna, *Angew. Chem., Int. Ed.*, 2014, **126**, 12802–12807.
10 Y. Chen, S. Xu, Y. Li, R. Jacob, Y. Kuang, B. Liu, Y. Wang, G. Pastel, L. Salamanca, M. Zachariah and L. Hu, *Adv. Energy Mater.*, 2017, **7**, 1700482.
11 L. Feng, G. Yu, Y. Wu, G. Li, H. Li, Y. Sun, T. Asefa, W. Chen and X. Zou, *J. Am. Chem. Soc.*, 2015, **137**, 14023–14026.
12 C. Xie, D. Yan, H. Li, S. Du, W. Chen, Y. Wang, Y. Zou, R. Chen and S. Wang, *ACS Catal.*, 2020, **10**, 11082–11098.
13 T. Wang, H. Xie, M. Chen, A. Aloia, J. Cho, G. Wu and Q. Li, *Nano Energy*, 2017, **42**, 69–89.
14 C. Yang, H. Zhao, Y. Hou and D. Ma, *J. Am. Chem. Soc.*, 2012, **134**, 15814–15821.
15 S. Li, R. Cao, M. Xu, Y. Deng, L. Lin, S. Yao, X. Liang, M. Peng, Z. Gao, Y. Ge, J. Liu, W. Li, W. Zhou and D. Ma, *Natl. Sci. Rev.*, 2022, **9**, nwab026.
16 X. Yang, J. Nash, J. Anibal, M. Dunwell, S. Kattel, E. Stavitski, K. Attenkofer, J. Chen, Y. Yan and B. Xu, *J. Am. Chem. Soc.*, 2018, **140**, 13387–13391.
17 Y. Liu, D. Tian, A. Biswas, Z. Xie, S. Hwang, J. Lee, H. Meng and J. Chen, *Angew. Chem., Int. Ed.*, 2020, **59**, 11345–11348.
18 Z. Wu, X. Li, W. Liu, Y. Zhong, Q. Gan, X. Li and H. Wang, *ACS Catal.*, 2017, **7**, 4026–4032.
19 Y. Li, S. Li, J. Hu, Y. Zhang, Y. Du, X. Han, X. Liu and P. Xu, *J. Energy Chem.*, 2021, **53**, 1–8.
20 J. Peto, T. Ollar, P. Vancso, Z. Popov, G. Magda, G. Dobrik, C. Hwang, P. Sorokin and L. Tapaszto, *Nat. Chem.*, 2018, **10**, 1246–1251.
21 H. Liu, Z. Liu, F. Wang and L. Feng, *Chem. Eng. J.*, 2020, **397**, 125507.
22 Z. Yu, Y. Xie, B. Xie, C. Cao, Z. Zhang, H. Huo, Z. Jiang, Q. Pan, G. Yin and J. Wang, *Energy Storage Mater.*, 2020, **25**, 416–425.
23 W. Liu, E. Hu, H. Jiang, Y. Xiang, Z. Weng, M. Li, Q. Fan, X. Yu, E. Altman and H. Wang, *Nat. Commun.*, 2016, **7**, 10771.
24 Z. Wu, L. Huang, H. Liu, M. Li and H. Wang, *Nano Res.*, 2020, **14**, 2264–2267.
25 H. Sun, C. Tung, Y. Qiu, W. Zhang, Q. Wang, Z. Li, J. Tang, H. Chen, C. Wang and H. Chen, *J. Am. Chem. Soc.*, 2022, **144**, 1174–1186.
26 S. Li, C. Xi, Y. Jin, D. Wu, J. Wang, T. Liu, H. Wang, C. Dong, H. Liu, S. Kulinich and X. Du, *ACS Energy Lett.*, 2019, **4**, 1823–1829.
27 D. He, Z. Li and J. Yuan, *Micron*, 2015, **74**, 47–53.
28 S. Kalavathi, S. Amirthapandian, S. Chandra, P. Sahu and K. Sahu, *J. Phys.: Condens. Matter*, 2014, **26**, 015601.
29 Z. Wang and Y. Jiang, *Micron*, 2000, **31**, 571–580.
30 Z. Chen, L. Cai, X. Yang, C. Kronawitter, L. Guo, S. Shen and B. Koel, *ACS Catal.*, 2018, **8**, 1238–1247.
31 S. Lyapin, A. Utyuzh, A. Petrova, A. Novikov, T. Lograsso and S. Stishov, *J. Phys.: Condens. Matter*, 2014, **26**, 396001.
32 J. Li, Z. Xia, M. Zhang, S. Zhang, J. Li, Y. Ma and Y. Qu, *J. Mater. Chem. A*, 2019, **7**, 17775–17781.
33 P. Shvets, O. Dikaya, K. Maksimova and A. Goikhman, *J. Raman Spectrosc.*, 2019, **50**, 1226–1244.
34 P. Vilanova, J. Hernánde, A. Landa and F. Agulló, *J. Alloys Compd.*, 2016, **661**, 122–125.
35 S. Zhang, L. Zhang, G. Xu, X. Zhang and A. Zhao, *New J. Chem.*, 2020, **44**, 10918–10923.
36 X. Wang, X. Zhong, Z. Zha, G. He, Z. Miao, H. Lei, Q. Luo, R. Zhang, Z. Liu and L. Cheng, *Appl. Mater. Today*, 2020, **18**, 100464.

 

37 S. Niu, S. Li, Y. Du, X. Han and P. Xu, *ACS Energy Lett.*, 2020, **5**, 1083–1087.
38 J. Wu, Z. Yu, Y. Zhang, S. Niu, J. Zhao, S. Li and P. Xu, *Small*, 2021, **17**, e2105150.
39 R. Hu, Y. Liao, H. Qiao, J. Li, K. Wang, Z. Huang and X. Qi, *Ceram. Interfaces*, 2022, **48**, 23498–23503.
40 X. Wang, H. Li, H. Li, S. Lin, W. Ding, X. Zhu, Z. Sheng, H. Wang, X. Zhu and Y. Sun, *Adv. Funct. Mater.*, 2020, **30**, 1910302.
41 Y. Lin, K. Sun, S. Liu, X. Chen, Y. Cheng, W. Cheong, Z. Chen, L. Zheng, J. Zhang, X. Li, Y. Pan and C. Chen, *Adv. Energy Mater.*, 2019, **9**, 1901213.
42 L. Yu, I. Mishra, Y. Xie, H. Zhou, J. Sun, J. Zhou, Y. Ni, D. Luo, F. Yu, Y. Yu, S. Chen and Z. Ren, *Nano Energy*, 2018, **53**, 492–500.
43 W. Xu, N. Apodaca, H. Wang, L. Yan, G. Chen, M. Zhou, D. Ding, P. Choudhury and H. Luo, *ACS Catal.*, 2019, **9**, 5074–5083.
44 Z. Yu, H. Shan, Y. Zhong, X. Zhang and G. Hong, *ACS Energy Lett.*, 2022, **7**, 3151–3176.
45 Z. Yu, X. Zhang, C. Fu, H. Wang, M. Chen, G. Yin, H. Huo and J. Wang, *Adv. Energy Mater.*, 2021, **11**, 2003250.
46 G. Kress and J. Furthmuller, *Comput. Mater. Sci.*, 1996, **6**, 15–50.
47 G. Kress and J. Furthmuller, *Phys. Rev. B: Condens. Matter Mater. Phys.*, 1996, **54**, 11169.
48 J. Perdew, K. Burke and M. Emzerhof, *Phys. Rev. Lett.*, 1996, **77**, 3865.
49 G. Kresse and D. Joubert, *Phys. Rev. B: Condens. Matter Mater. Phys.*, 1999, **59**, 1758.
50 P. Blochl, *Phys. Rev. B: Condens. Matter Mater. Phys.*, 1994, **50**, 17953.